Measurement 117 (2018) 347–364

Contents lists available at ScienceDirect

Measurement

journal homepage: www.elsevier.com/locate/measurement

3-D monitoring of rubble mound breakwater damages

Rosaria E. Musumeci[a,*], Davide Moltisanti[b], Enrico Foti[a], Sebastiano Battiato[b], Giovanni M. Farinella[b]

[a] Department of Civil Engineering and Architecture, University of Catania, Viale Andrea Doria 6, Catania, Italy
[b] Image Processing Laboratory, University of Catania, Viale Andrea Doria 6, Catania, Italy

ARTICLE INFO

Keywords:
RGB-D cameras
Optical measurements
Accropodes
Underwater measurements

ABSTRACT

Breakwaters play a crucial role in the protection of coastal zones. Their maintenance is critical to safeguard the daily activities of harbours and marine areas. The evaluation of damage is a necessity for timely preservation works. Traditional monitoring methods span various techniques, ranging from mechanical profilers to optical systems. Current methods though are expensive, requiring remarkably sophisticated technologies which demand a high degree of expertise to be operated.

In this paper, we propose an affordable yet accurate fully automated method based on 3D cameras. Our technique is non invasive, allowing hence non intrusive as well as fast measure of damage over time, simultaneously above and below sea water level. Experimental results obtained on laboratory breakwater models demonstrated that the proposed point cloud method, which does not depend on the imaging sensor and can be applied to any 3D dataset of rubble mound breakwater, can achieve accurate damage estimation, even when using a budget RGB-D camera. One of the additional advantages of using RGB-D cameras is the possibility to obtain measurements also in the presence of water.

1. Introduction and motivation

Breakwater structures are used worldwide to protect harbours and coastal zones from wave attack. Depending on the local availability of materials, on the bathymetric conditions, on the wave climate and on specific design requirements, breakwaters can be built by using rocks or concrete units, located as a double or single layer, considering a traditional trapezoidal shape or a berm breakwater, with different types of toe structures.

Due to the large site-dependent construction variability, the damage estimation of rubble mound breakwaters is a delicate and a crucial task. Notwithstanding the advances of numerical CFD models able to simulate the flow between individual blocks of the armour layer [1], laboratory experiments remain the most reliable methodology of investigation due to the complexity of the interactions between the flow and the armour layer units, the filter layer, the toe and the core of the actual structure. Indeed, several empirical approaches have been proposed based on laboratory experiments - [2–9] just to list a few - and are currently used as a basis for the design of rubble mound breakwaters.

Stability formulae are usually expressed in terms of the stability parameter $H_s/\Delta D_{n50}$, where H_s is the significant wave height, $\Delta = \rho_r/\rho_w - 1$ is the relative density with ρ_r and ρ_w being respectively the rock and water density, and D_{n50} is the median diameter of rock armour units or some characteristic dimension of concrete elements. Traditionally, the damage to the armour layer of the breakwater is expressed as the damage percentage N_d of displaced stones related to a certain area, which could be a part of the armour layer or the entire layer itself. Another approach considers the damage level S, i.e. the ratio between the erosion area around the still-water level A_e, and D_{n50}^2. The above parameters can be considered as complementary. The first parameter is focused on the armour layer exposed surface, while the second parameter accounts for deformation of the overall breakwater cross-section.

Concerning the measurement of the damage to the structure, a long time has passed since the pioneering work of Hudson [2], who measured the cross-sections by using a sounding rod equipped with a circular spirit level, a graduated scale and a ball-and-socket foot. Nowadays, in hydraulic laboratories the measurement of armour layer damage is generally performed through mechanical or laser profiling [9–13] or visually by means of video cameras [6,8,9,14–16].

Mechanical profilers are usually preferred when large models with significant damages are considered. The use of profilers, though very accurate, requires that the experiment is stopped, therefore dynamic

* Corresponding author.
E-mail addresses: rmusume@dica.unict.it (R.E. Musumeci), davidemoltisanti@gmail.com (D. Moltisanti), efoti@dica.unict.it (E. Foti), battiato@dmi.unict.it (S. Battiato), gfarinella@dmi.unict.it (G.M. Farinella).

https://doi.org/10.1016/j.measurement.2017.12.020
Received 31 July 2017; Received in revised form 12 December 2017; Accepted 13 December 2017
Available online 19 December 2017
0263-2241/

observations cannot be obtained. Moreover, often several profiles need to be measured in the spanwise direction, in order to obtain average or maximum estimates of the damage along the breakwater length [12,13]. This is to avoid under- or over-estimates of the damage levels, depending on the position of the control section in the flume.

Photographic techniques are quite popular because outcomes of experimental studies are provided in a form which is closer to the operator's perception, allowing thus an easier interpretation of the data under analysis. Several applications of optical methodologies are possible, the most common being the overlap of photos to determine rock and concrete unit movements, while videos can help to identify instability mechanisms. However, image techniques usually require a reliable calibration. Moreover, they are generally limited to the two-dimensional observation of the armour layer, either from the top or from the side. Furthermore, measurements below the water surface may be difficult. For example, Vidal et al. [10] compared three different methodologies to assess damages to rubble mound breakwaters, in terms of the damage level S, namely (i) laser profiling, (ii) to count settled stones in more than two layers and (iii) digital image processing counting pixels of layer below the outer armour layer. Such authors demonstrated that profiling techniques are more accurate for larger damages and that calibrated image analysis techniques can underestimate damage levels, particularly if the second layer is affected. It is worth noting that in order to understand the failure mechanism of the structure, it is important to consider not only damage levels but also damage progression [16,17]. Therefore dynamic measurements over large portions of the breakwater are necessary.

The importance of gathering objective measurements of the armour layer damage was underlined by Chilo and Guiducci [18], who proposed a manual image processing to recover small armour unit movements. More recently, van Gent and van der Werf [19] used stereo photography when investigating the stability of rock toes. However, such authors state that they used the 3D map of the structure just for a quick verification of the damage values obtained through profiling.

In general, traditional photographic techniques, such as laser scanner or stereo-photogrammetry methods, are able to provide a three-dimensional damage assessment without interacting with the structure. However, in order to obtain measurements below water level, the structure has to be drained by emptying the wave flume. Such a procedure causes longer experimental time and it may even affect the stability of the structure, particularly in the presence of sandy beds. Moreover, calibration of stereo-systems and automation of photogrammetric techniques are not trivial tasks, needing a lot of time to be finalised. Furthermore, costs of stereo-system or of laser scanner systems may be relatively high.

A different class of three-dimensional optical systems is represented by Red-Green-Blue and Depth (RGB-D) cameras. RGB-D cameras are low cost technologies which can see both under and above the water, combining in only one device the capability to observe the whole structure. The high-fidelity dense topographic/bathymetric point cloud allows a whole new group of analyses and data to be employed. This level of detail and the magnitude of data imply a challenging new approach to the way data are stored, processed and presented. While sensor systems with these capabilities have been custom-built for long time, it has been only recently that they are being available in affordable and consumer forms, which make them attractive for research outside specialised computer vision groups [20–22].

In this work a novel three-dimensional laboratory technique based on RGB-D cameras is proposed to measure rubble-mound breakwater damage simultaneously above and below sea water level. In particular, here the proposed monitoring method is applied to the investigation of the stability of an Accropode breakwater under wave attack. The potentialities of the proposed technique are pointed out by using traditional and new methodologies to describe the structure damages.

In particular, Accropodes belong to the category of single-layer concrete armour blocks. They are quasi-randomly placed, according to a well-defined positioning of their centre of mass and to some construction rules-of-thumb aimed at ensuring the maximum level of interlocking [23]. Their behaviour is quite different from that of double-layer elements. Indeed, the packing of the elements is completed under the wave attack and the system acts as an integral layer [5]. The work in Kobayashi and Kaihatsu [24] investigated experimentally the performance of Accropodes, reporting good stability characteristics for this type of blocks based also on field experience. However the authors underline the fact that although the stability at no damage condition was very high, the criteria of no damage and failure were very close. This was also confirmed by van der Meer [4], who suggests the following criteria for initiation of damage and failure respectively:

$$\frac{H_s}{\Delta D_n} = 3.7 \tag{1}$$

$$\frac{H_s}{\Delta D_n} = 4.1 \tag{2}$$

where H_s is the significant wave height, Δ is the relative submerged specific gravity of the blocks and D_n is the nominal diameter of the blocks. Both coefficients have a standard deviation of $\sigma = 0.2$. van der Meer [4] suggests that the criterion for the starting of damage must not be considered for design, and a different formula for design is proposed by van der Meer [25]:

$$\frac{H_s}{\Delta D_n} = 2.5 \tag{3}$$

This will include a safety coefficient which reduces the risk of failure induced by underprediction of the expected design wave height [5].

From the above considerations, it follows that it is extremely important to accurately monitor even the smallest movements of each single Accropode element, as the overall stability of the armour layer could be compromised. Therefore, the investigation of such kind of structures represents an ideal case to test the capabilities of the proposed fully automatic damage assessment methodology. Indeed, on one hand Accropode elements have a regular geometry, on the other side their stability curve is very steep [4,25], hence a measurement technique must be able to accurately detect any tiny deformation or rocking of the armour units. In particular, the roto-translation movements of the armour layer are estimated by means of the proposed RGB-D technique. Such results allow to diagnose the mechanism of failure, by identifying the weakest part of the armour layer, from which a structure collapse could suddenly develop.

The work is organised as follows. In Section 2 we introduce the proposed measuring system. Section 3 provides an overview of the adopted RGB-D technology and a quantitative assessment of the measuring errors of the depth cameras in the application context is carried out. In Section 4 details regarding the experimental campaign setup are provided. In Section 5 we discuss the results of the proposed methodology, whereas in Section 6 we compare such results with traditional methods. Finally, Section 7 provides conclusions and hints for future works.

2. Proposed measuring system

RGB-D technology refers to three-dimensional reconstruction of the observed scene, that is the acquisition of traditional RGB data along with per-pixel depth information (i.e. the distance of the points in the scene from the camera). There are several techniques tackling this challenging task. Stereo-based methods try to match corresponding points in a image pair coming from a stereo camera, basing the calculation of the depth on the relative distance of the matching points in the two images [26]. Structured light approaches project an "invisible" light pattern onto the scene and infer the depth map by measuring the deformation of the reflected pattern [27–30]. The depth of the scene

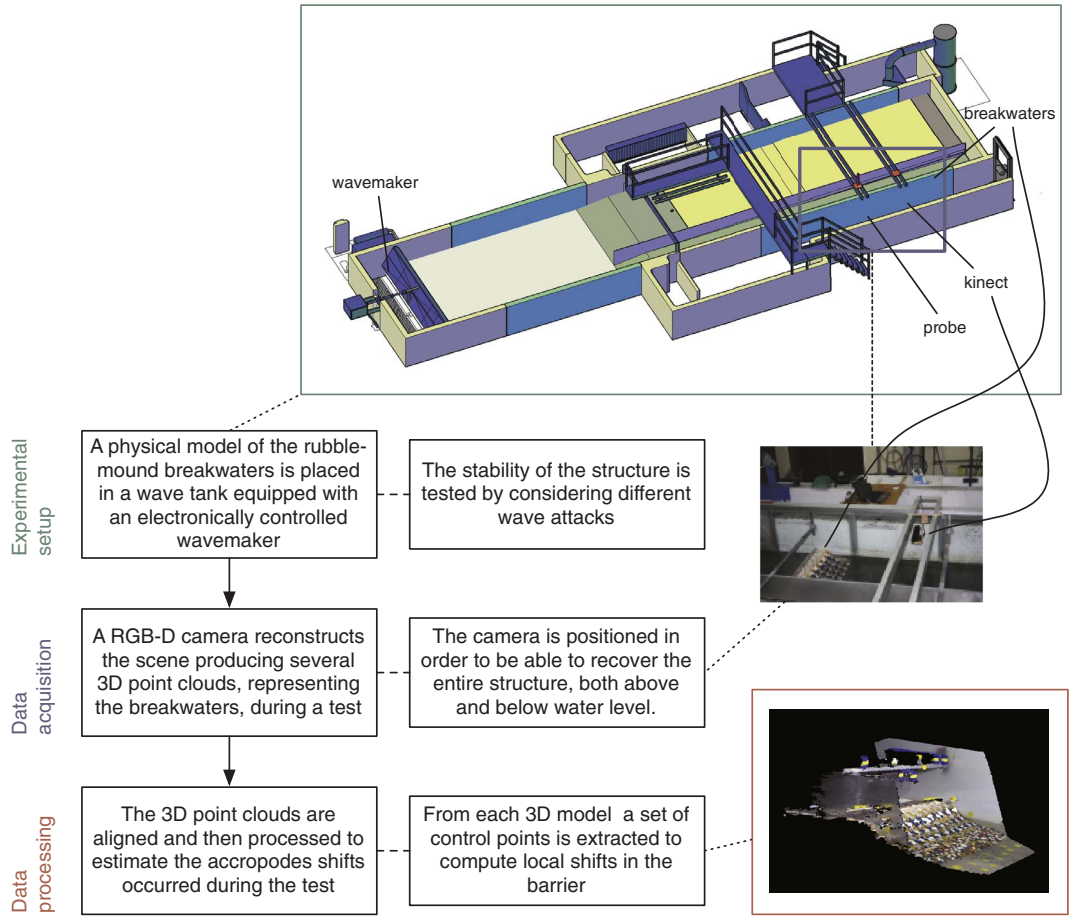

Fig. 1. Generic pipeline of the proposed approach. The pipeline is divided in three main modules: experimental setup, data acquisition and data processing.

can also be measured using time-of-flight techniques, where the distance of the points is obtained by measuring the time of flight of a light signal reflected by the surface [31,32].

The pipeline of the proposed measuring system is illustrated in Fig. 1. During the experiments a physical model of a rubble-mound breakwater is hit by waves to test the stability of the structure. Several 3D point cloud models of such structure are acquired with a RGB-D camera, in order to monitor the conditions of the breakwater and estimate the evolution of damage during wave storm attack. The camera was mounted perpendicularly to the analysed surface. The 3D models are hence processed to estimate the movements of the armour layer blocks. Experimental setup and the data acquisition procedure details are provided in Section 4, whereas in the following the proposed measuring method is presented.

2.1. Automatic 3D data processing and measurements

The workflow of the data processing is illustrated in Fig. 2. Top row pictures show the breakwater being hit by a sequence of waves during a test. The corresponding 3D reconstructions are illustrated below. We call “clouds” the ordered list of meshes that have been reconstructed during an experiment: the *i*-th 3D model captured at time *i* is stored at position *i* of the clouds list. A “special” cloud is that stored at position 0: this is the mesh of the initial condition of the barrier, that is before the experiment started. The cloud at time 0 is used as reference mesh to evaluate movements in every subsequent cloud at time *i*-th. The first step in the processing pipeline is related to the alignment of the cloud *i*-th with respect to the reference cloud, as discussed below. Thereafter, we evaluate blocks movements by calculating local differences between the point clouds, as explained in Section 2.3.

2.2. Point clouds alignment

3D models belonging to the same testing sequence may be not aligned, that is the models may not overlap exactly one with the other. This can occur due to slight vibrations transmitted to the RGB-D camera by the waves during the experiment, causing thus minor shifts of the camera.

Every clouds(*i*) of the test sequence is aligned with respect to the reference clouds(0), using the Iterative Closest Point algorithm [33], considering specific sub-clouds parts selected by the user on the reference mesh. A sub-cloud is a mesh composed of subsets of points of the source cloud. We call this sub-cloud “ICP-cloud”: ICP-cloud(0) refers then to the sub-cloud of the reference clouds(0), while ICP-cloud(*i*) refers to the *i*-th cloud of the sequence. In particular, for the alignment algorithm we pick those parts of the clouds where no movements can occur (e.g. fixed frame bars or lateral flume walls). Given that ICP operates by finding matches between points and minimising their distance in the Euclidean space, a region where some movements take place would lead to a failure of the alignment algorithm. Fig. 3 illustrates an example of such region, marked in red. In this part of the cloud the elements of the armour layer, which move both slightly and considerably, are located according to the intensity of the flooding waves. In Fig. 3, the steel rod at the bottom of the barrier is marked too; this is because some blocks may fall down and get to the bottom due to a barrier break. In these cases, by considering those part for the alignment, the ICP procedure would fail as the matching between the reference mesh and the cloud to be aligned would fail.

Fig. 4 depicts the building phase of an ICP-cloud. The software asks the user to pick some spheres located in the correspondence of static structures from the reference clouds(0): the points lying inside the red

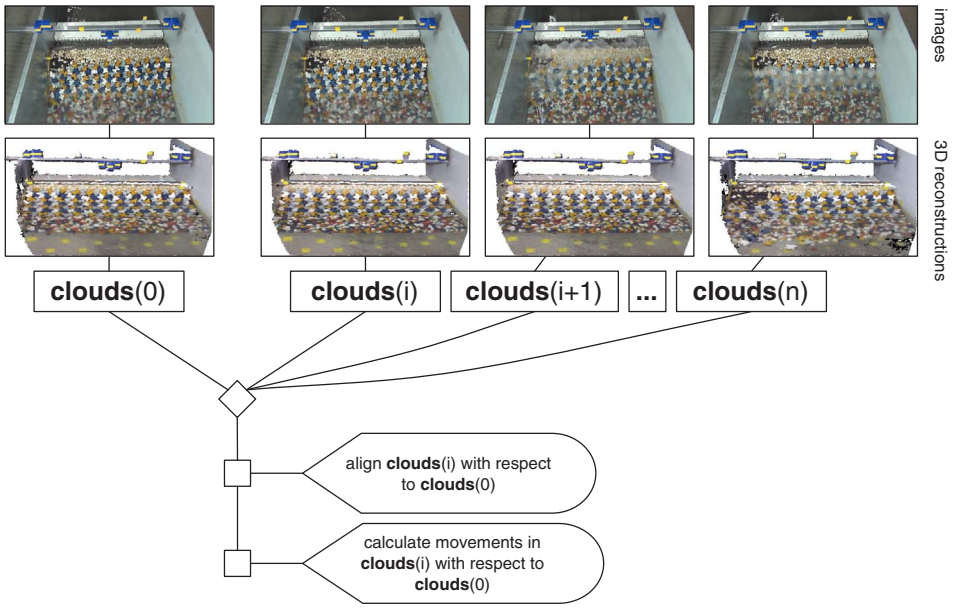

Fig. 2. Workflow of the proposed approach. The pictures at the top row show the breakwater model under wave attack during a test, in relationship with the corresponding 3D reconstructions, which are located at the bottom row. A damage on the top left part of the barrier is visible in the last 3D reconstruction/picture of the sequence.

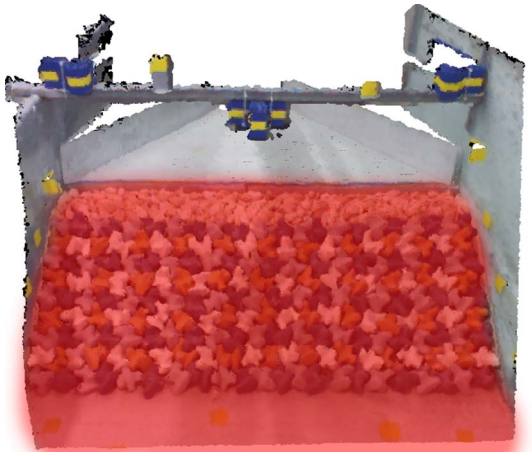

Fig. 3. Region of a cloud where movements can take place (marked in red). (For interpretation of the references to colour in this figure legend, the reader is referred to the web version of this article.)

spheres are extracted from the source cloud and put in the ICP-cloud. The sub-cloud is built asking the user only once per test sequence. Specifically, the ICP-cloud is built on the reference clouds(0): then, for every clouds(i) to be aligned, the corresponding ICP-clouds are created by taking those points in clouds(i) which lie in the spheres defined by the user. This means that the (x,y,z) coordinates of each sphere centre are referred to clouds(0) space and are the same every time an ICP-cloud is created; given that the meshes may be slightly shifted each other, though, the points lying inside the spheres might change a little in every clouds(i). We find these shifts with the ICP algorithm and we then apply the resulting transformation matrix to the clouds(i). For each couple [clouds(0), clouds(i)], after the creation of the corresponding ICP-clouds, the system runs the ICP algorithm, which can be resumed as follows:

1. For each P_i^k point in ICP-cloud(i), find the nearest point P_0^k in ICP-cloud(0).
2. Estimate the roto-translation matrix M which best aligns P_i^k points to the corresponding P_0^k. The matrix is evaluated by calculating the Mean Square Error (MSE) over each point.
3. Apply the transformation matrix M to clouds(i).
4. Repeat from point (1) until a stop criterion is satisfied.

ICP has three stop criteria:

1. A certain number of iteration is reached.
2. The difference between the previous transformation and the current estimated transformation is smaller than a certain value.
3. The sum of Euclidean squared errors is smaller than a defined threshold.

In all our experiments both criteria 1 and 3 have been used jointly, setting 100 as maximum number of iterations and 10^{-8} as threshold for the Euclidean squared errors sum. In Fig. 5 we can observe the result of the alignment process between two clouds.

2.3. Calculating movements of the armour layer elements

After the alignment phase, the next step in the workflow is the evaluation of the roto-translation movements of the elements of the armour layer. First, the reference clouds(0) is subsampled dividing its space in cubes of side n (which is set by default equal to 2 cm). For each cube j the points contained in it are substituted and represented by their mass centre P_j. These P_j points are used as control points to calculate both rotational and translational shifts between the reference cloud and a mesh clouds(i) from the sequence. Fig. 6 illustrates a result of such subsampling process. Every point showed in this mesh represents a control point P_j, that is the mass centre of the points contained in the corresponding j-th cube of the cloud.

2.3.1. Translation estimation

To estimate translation shifts for a clouds(i), we run a radius search around each mass centre P_j:

- For each $P_j = (x_j,y_j,z_j)$, find in clouds(i) the points lying in the neighbourhood given by the sphere of radius $\frac{n}{2}$ and centre P_j. Let $neighbours(P_j)$ be the set of these points.
- Calculate the mass centre P'_j for the points in $neighbours(P_j)$.
- The movements occurred in the space portion of clouds(i) located by the sphere centred in P_j is given by the Euclidean distance between P_j and P'_j.

We use K-d tree [34] implementation of the Point Cloud Library to run radius search over the clouds. Fig. 7 provides a graphical example of application of the radius search based algorithm.

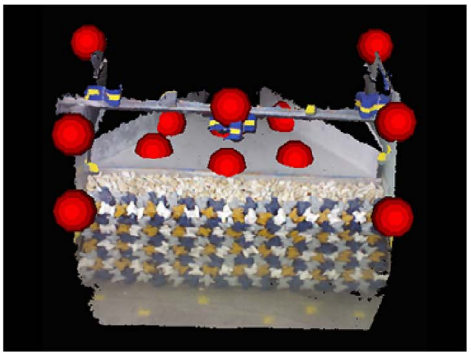

(a) Spheres of points picked by the user

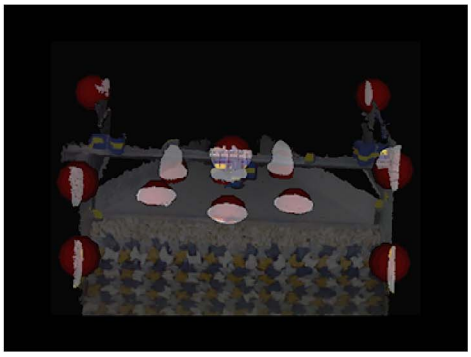

(b) Overlap between the picked spheres and the resulting ICP-cloud

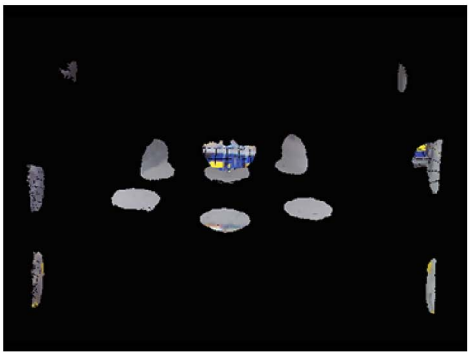

(c) The resulting ICP-cloud

Fig. 4. ICP-cloud for the reference mesh. (a) The user selects some spheres in static regions where no movements can occur, such as the bar upon the barrier, the walls and the rod beyond the breakwater. The points included in these spheres will populate the ICP-cloud. In (b) the reference clouds(0) is superimposed over the points included by the spheres, so that we can observe the points that are extracted to create the ICP-cloud, which is shown in (c). The diameter of the spheres can be adjusted and is set by default to 7 cm.

2.3.2. Rotation estimation

Mesh surface normals are computed in order to estimate the rotation of the armour blocks for a clouds(i). More precisely, to calculate the rotation in a portion of a clouds(i) located by a control point P_j, we proceed as follows:

- Given the point $P_j = (x_j, y_j, z_j)$, estimate in clouds(0) the normal vector $\overrightarrow{N_0}(j)$ of the surface given by the points lying on the spherical neighbourhood of radius $\frac{n}{2}$ and centre P_j.
- Estimate in clouds(i) the normal vector $\overrightarrow{N_i}(j)$ of the surface given by the points lying on the spherical neighbourhood of radius $\frac{n}{2}$ and centre P_j.
- The angle θ between $\overrightarrow{N_0}(j)$ and $\overrightarrow{N_i}(j)$ vectors gives an estimate of the rotation occurred in the portion of clouds(i) located by P_j.

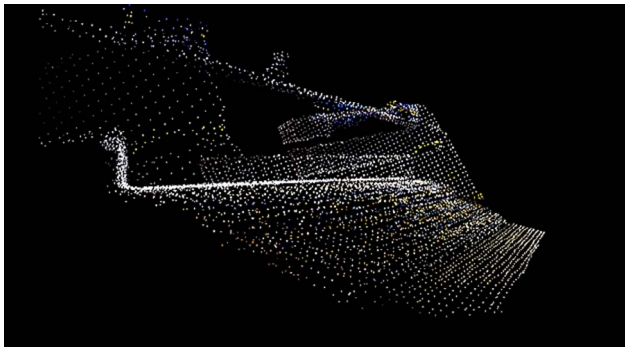

Fig. 6. Point Cloud subsampling result.

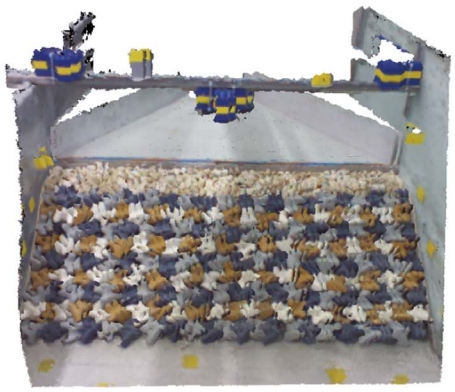

(a) Overlapped 3D models before alignment

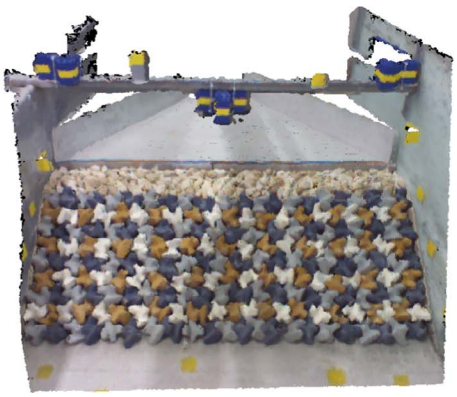

(b) Overlapped 3D models after alignment

Fig. 5. Clouds alignment. (a) Before the alignment process, a noticeable shift between the overlapped 3D models is clearly visible. (b) After the alignment, the clouds are perfectly overlapping and the two meshes are not distinguishable.

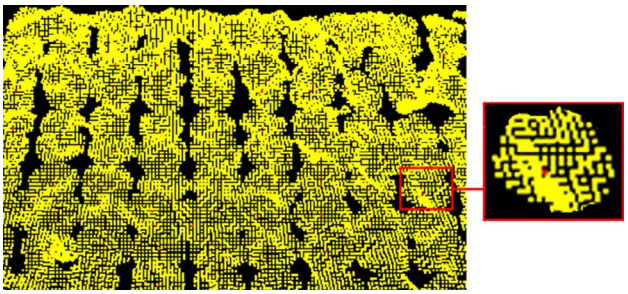

Fig. 7. Radius search. The red dots represent all the control points P_j, whereas the yellow dots represent the points lying in *neighbourhood*(P_j). In the right part a single control point and its respective neighbourhood is isolated: here it's quite visible that the mass centre of the yellow points doesn't coincide with the control point P_j. This means that a shift has taken place in that portion of the cloud, which will be estimated as the Euclidean distance between P_j and the mass centre of *neighbourhood*(P_j). The radius of the sphere containing the yellow points, i. e. the radius of the neighbourhood search, is an adjustable parameter of the algorithm which is set by default to 2 cm. (For interpretation of the references to colour in this figure legend, the reader is referred to the web version of this article.)

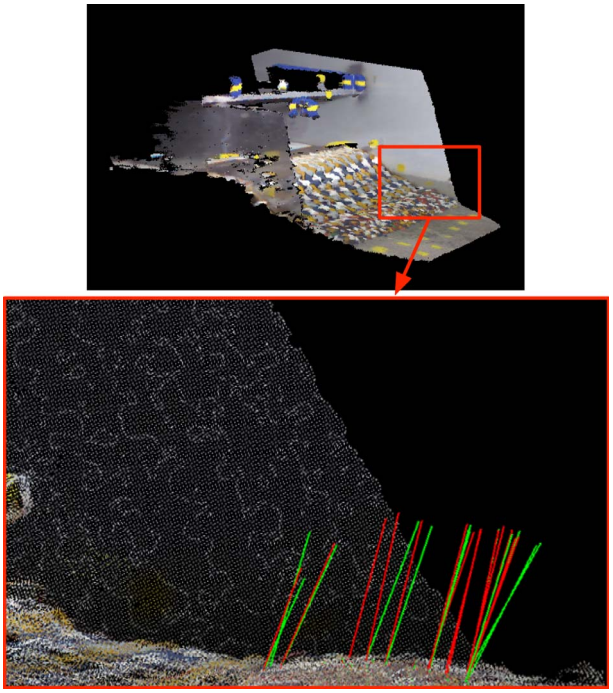

Fig. 8. Estimation of the normals and comparison on a portion of mesh. Green lines are normal vectors computed for the reference cloud, while red lines are normals vectors computed for a cloud in the sequence. For clarity sake only a subset of vectors is illustrated. (For interpretation of the references to colour in this figure legend, the reader is referred to the web version of this article.)

To calculate the angle between $\overrightarrow{N_0}(j) = (A_1,B_1,C_1)$ and $\overrightarrow{N_i}(j) = (A_2,B_2,C_2)$, the angle between their perpendicular planes is considered:

$$\theta(\overrightarrow{N_0}(j),\overrightarrow{N_i}(j)) = \arccos\frac{|A_1\cdot A_2 + B_1\cdot B_2 + C_1\cdot C_2|}{\sqrt{A_1^2 + B_1^2 + C_1^2}\cdot\sqrt{A_2^2 + B_2^2 + C_2^2}} \quad (4)$$

We estimate normal vectors using the method proposed in Berkmann and Caelli [35], which is based on Principal Component Analysis. Fig. 8 illustrates an example of estimate of the normals and comparison of a couple [clouds(0), clouds(i)], considering only a small region of the mesh. Red lines are $\overrightarrow{N_i}(j)$ vectors, while green lines are $\overrightarrow{N_0}(j)$ vectors; the mesh depicted in the picture is the reference cloud. In this example almost every $\overrightarrow{N_i}(j)$ vector is parallel to the correspondent reference vector $\overrightarrow{N_0}(j)$, since no noticeable movements have occurred in this part of clouds(i). In contrast, when the vectors are not parallel a significant rotation has occurred.

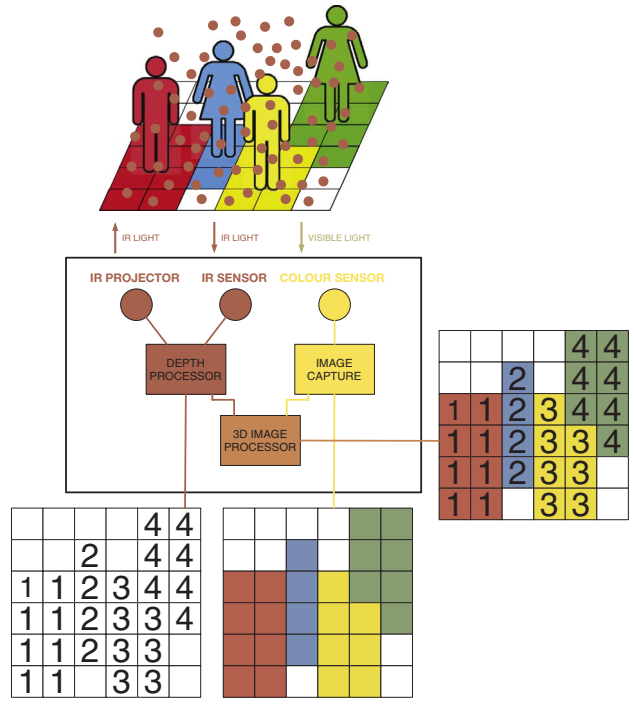

Fig. 9. Kinect scheme. The red dots scattered over the stick men represent the infrared pattern projected by the Kinect. Depth map and image capture are matched together to create a unique 3D image of the scene. (For interpretation of the references to colour in this figure legend, the reader is referred to the web version of this article.)

3. Adopted RGB-D technology

The widely known low-cost Microsoft Kinect camera was used as RGB-D camera in our experiments.[1] Microsoft Kinect sensor belongs to the family of RGB-D devices which reconstruct the depth of a scene by using an infrared (IR) light pattern [36]. In order to create the depth map, the Kinect's IR projector throws a bundle of pseudo-random infrared beams. The reflected rays are captured by the infrared camera, and a 3D reconstruction algorithm determines how the points are close to the device. The depth map of the scene is provided as an image M of $m \times n$ size, where each pixel $p(x,y)$ encodes the distance in the scene of the 3D point from the sensor. Fig. 9 illustrates the Kinect scene reconstruction procedure.

The structured light technique used by the Kinect exploits a stereo vision system built by coupling the projector and the camera. A known infrared pattern is projected into the scene and the depth of the objects is computed by measuring its distortion on the objects. It is possible to implement this technique with various methods. A first approach is the projection of lines and the measuring of their curvature on objects. Such a technique is not very fast and it is also subject to interference when objects are in motion. A second possibility is the projection of 2D periodic patterns and the evaluation of their deviation on hit objects. In this way the 3D information is obtained in real-time but the sensor cannot work over long distances because of the pattern distortion. A third method, which is the one used by Kinect, is the projection of 2D pseudo-random patterns. The advantage of this method is the possibility to obtain accurate real-time 3D maps thanks to the pattern randomness, despite their two-dimensionality.

[1] We used the first edition of Kinect for Windows.

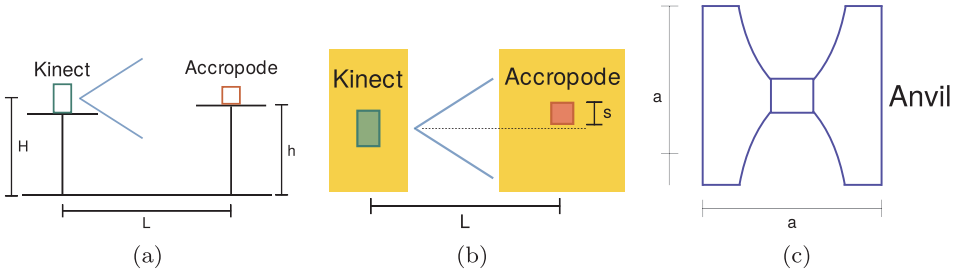

Fig. 10. Kinect-Accropode configuration for the accuracy evaluation experiments in static conditions. Side view and top view of the experimental setting are depicted respectively in (a) and (b). (c) The Accropode position assumed during the performed tests.

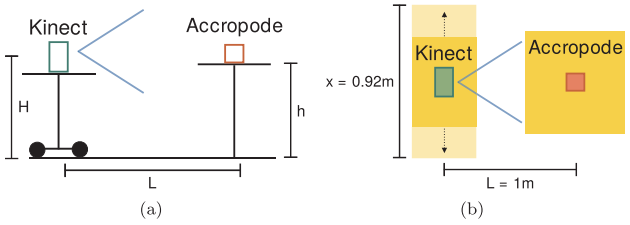

Fig. 11. Kinect-Accropode configuration for the accuracy evaluation experiments in dynamic conditions. Side view and top view of the experimental setting are depicted respectively in (a) and (b).

3.1. RGB-D system settings and measuring capabilities

In order to use the Kinect sensor to monitor the damage of rubble mound structures in hydraulic laboratories, a preliminary assessment of the reconstruction accuracy was carried out. Such preliminary tests have proved useful to determine the optimal range of setting parameters of the Kinect sensor as well.

Every depth map was acquired with the Kinect Fusion Explorer software, which is part of the Microsoft Kinect SDK [37]. The volume of a 3D reconstruction is composed of small cubes which are referred to as "voxels". The most important parameters of a reconstruction, with respect to its accuracy, are the Volume Voxels Resolution (VVR), that is the total amount of voxels in the final 3D model and the Volume Voxels per Meter (VVPM), that is the spatial density of the reconstruction. Besides, another crucial parameter is the Volume Max Integration Weight (VMIW). This parameter controls the time averaging of data into the reconstruction volume: by increasing it, the system is able to reconstruct the scene with a higher detail but, at the same time, takes longer time to reconstruct the scene, and therefore does not adapt to quickly changing scenarios. Low values of the VMIW parameter make the system respond faster to changes in the scene (e.g. moving objects), but produces noisier results. Finally, the distance between the Kinect and the target object is a discriminative factor regarding the resulting 3D reconstruction. Depending on the size of the object, the range of distances which work best for the reconstruction can vary remarkably.

3.1.1. Accuracy evaluation on single Accropode reconstruction

In order to evaluate the accuracy of the Kinect reconstruction, we undertook an initial series of tests on a single physical Accropode model of dimensions O(5 cm). The purpose of these experiments was to find the Kinect configuration minimising the measurement error. The tests consisted in the 3D reconstruction of the analysed object and in the comparison of its real size with the acquired 3D model, both in static and dynamic conditions. In the former case the Kinect cameras was placed at a fixed location with respect to the Accropode, while in the latter case the Kinect was moved around the object.

The static tests on the single Accropode were initially performed considering the maximum allowed values of the parameters VMIW, VVPM and VVR, setting a constant distance between object and Kinect. The experimental configuration in static conditions is illustrated in Fig. 10, where L is the distance between the Kinect and the Accropode, H is the vertical distance of the Kinect from the floor, h is the distance of the Accropode and s is its lateral shift with respect to the lens axis. The Accropode is frontal with respect to the lens of the camera, as illustrated in Fig. 10(c) (the Accropode anvil is 0.0464 m high). This position was also maintained in the dynamic tests, which were performed with the use of a trolley, moving the Kinect along a rail.

The experimental configuration in dynamic conditions is illustrated in Fig. 11, where L, fixed to 1 m, is the distance between the Kinect and the Accropode, h is the height of the Accropode, and x, equal to 0.92 m, is the amplitude of the movement of the camera along the rail line during the 3D reconstruction. As for the static test case, both software and geometrical parameters of the experimental setting have been explored under dynamic conditions. More specifically, 120 tests were carried out in static conditions, while 60 were performed in dynamic conditions. In order to evaluate the measuring error, the anvil side was measured for each test in which the Accropode was identified. Given that the Accropode anvil is not univocally defined in the RGB-D meshes,

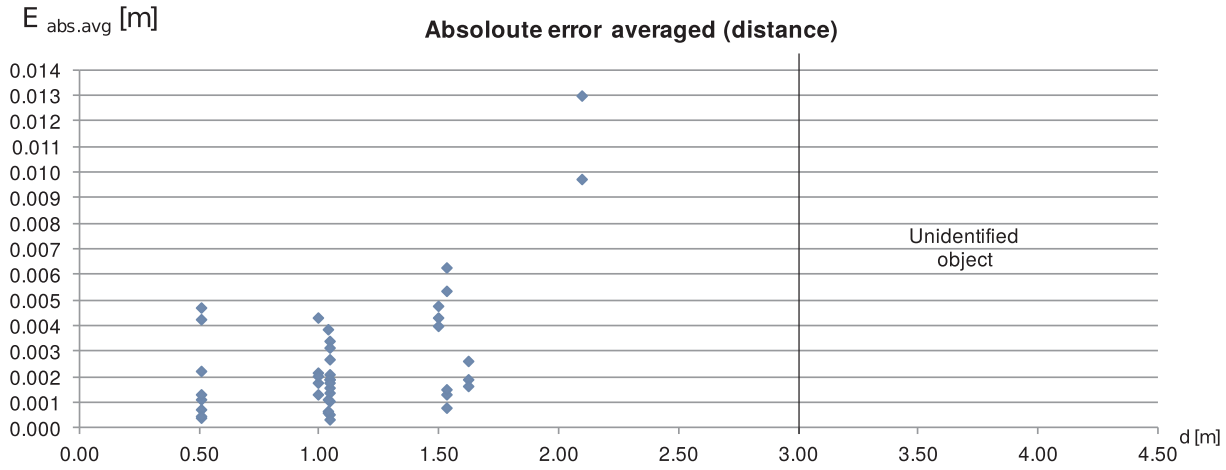

Fig. 12. Static tests: average absolute measuring error as a function of the distance of the Kinect camera from the Accropode model.

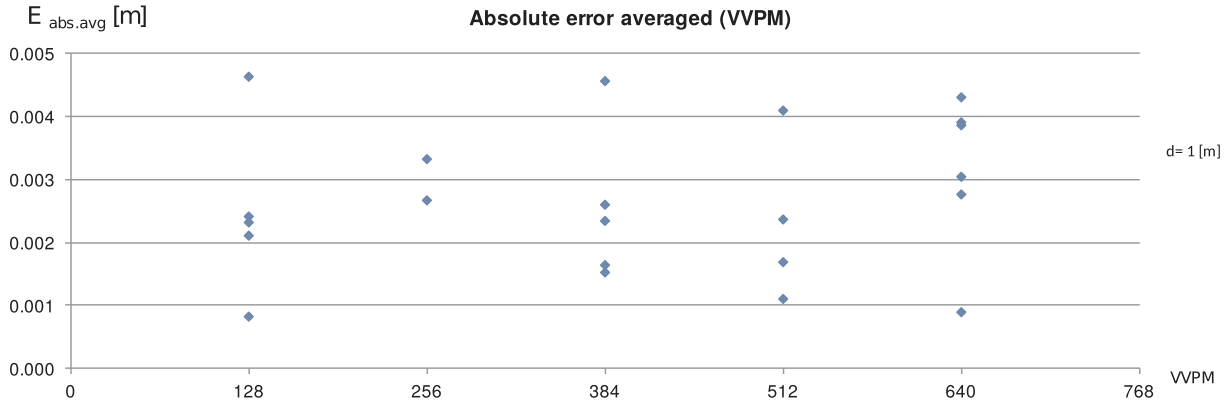

Fig. 13. Dynamic tests: average absolute error as a function of the VVPM parameter (distance between the camera and the object is equal to 1 m).

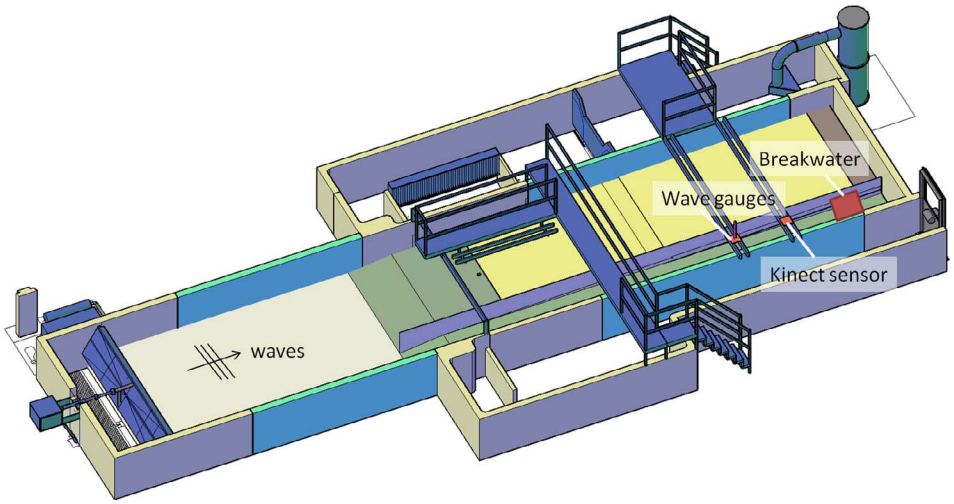

Fig. 14. Three-dimensional model of the experimental wave tank.

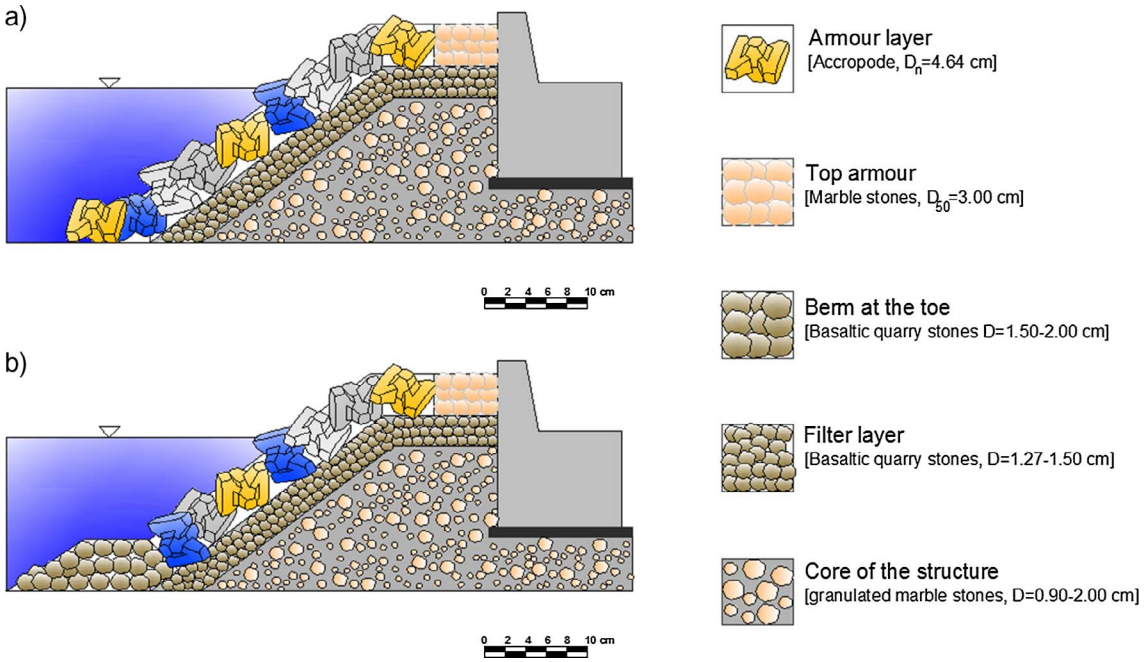

Fig. 15. Sections of the two investigated configurations of the breakwater: (a) configuration *A*, with Accropodes located both on the armour layer and at the toe of the structure; (b) configuration *B*, with Accropodes on the armour layer and a quarry stone berm.

Table 1
Experimental wave parameters. H_{si} and H_{sr} indicate respectively incident and reflected significant wave heights, mean wave period is indicated by T_m, whereas reflection coefficient is referred with K_r.

	Test	H_{si} [cm]	H_{sr} [cm]	T_m [s]	*Kr* [–]	*Ns* [–]
Configuration *A*	A01	2.81	1.06	0.50	0.38	1.53
	A02	6.87	1.92	0.70	0.28	3.74
	A03	6.61	1.89	0.80	0.29	3.60
	A04	7.02	2.43	0.81	0.35	3.82
	A05	7.20	2.91	0.84	0.45	3.92
	A06	7.28	3.07	0.85	0.42	3.96
	A07	7.01	3.00	0.88	0.43	3.81
Configuration *B*	B01	2.99	1.15	0.51	0.38	1.63
	B02	6.98	2.60	0.72	0.37	3.80
	B03	8.36	2.95	0.81	0.35	4.55
	B04	9.44	3.09	0.87	0.33	5.14
	B05	9.46	3.38	0.93	0.36	5.15
	B06	10.64	3.71	0.94	0.35	5.79
	B07	10.53	3.56	1.00	0.34	5.73
	B08	10.78	3.89	1.02	0.36	5.87
	B09	10.83	4.00	1.04	0.37	5.89
	B10	11.21	4.21	1.17	0.38	6.10

in order to check the influence of the operator we obtained multiple measurements by independent operators. Once the anvil measures were obtained, the absolute and the relative errors were calculated by all the operators. Subsequently, we calculated the average of these values, obtaining the mean absolute error and the mean relative error. All the data collected from every single test were used to analyse the distribution of the error as a function of the distance and of the VVPM values, in static conditions, and of the VIMW parameter in dynamic conditions.

By keeping the Kinect sensor fixed with respect to the observed object, we reconstructed a single Accropode model from 6 different distances of the camera, by setting for each of them only 5 possible values of the parameter VVPM. A total of 30 reconstructions were obtained. Specifically the nominal station positions of the Kinect camera were 400, 300, 200, 150, 100, and 50 cm. We did not collect measurements for distances greater than 400 cm, as this is the nominal capturing range of the Kinect (edition 1). In order to verify the camera performances in usual working conditions of hydraulic laboratories, the tests were repeated by slightly displacing the camera around the nominal station position. For example, at the nominal 1.00 m station, which is the most relevant in the present experimental conditions, four different actual distances have been used, namely 1.00 m, 1.01 m, 1.04 m, 1.09 m. On the other hand the VVPM values were set equal to 64, 128, 256, 384, 512, 640. Such preliminary tests showed that for distances greater than 300 cm, it was not possible to recognise the Accropode model in the reconstructed scene with any VVPM value. Considering distances equal to 150 and 200 cm, and values of VVPMs larger than 512 and 384 respectively, the Accropode element was not recognised either. For this reason, we focused on working distances smaller or equal to about 200 cm. Fig. 12 illustrates the outcomes of the tests carried out in static conditions, while Fig. 13 reports the results of the dynamic conditions tests. In particular, in static conditions the best reconstruction, with errors smaller than 0.003 m, is obtained at a distance equal to 1 m. As for the software parameters, the value which minimises the relative error is 640 for both the VVPM and the VVR (in all the three spatial directions). In dynamic conditions, where the distance was also set to 1 m, in many cases it was not possible to recognise the physical model of the Accropode in the scene and therefore it was

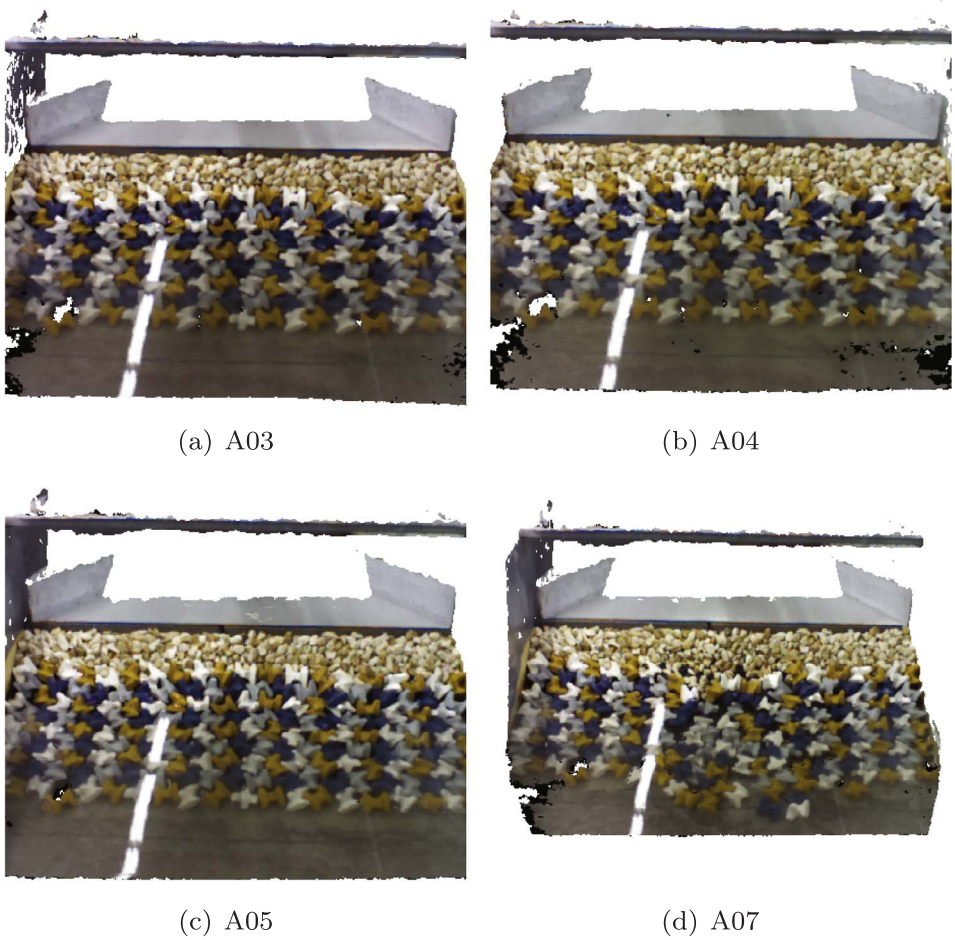

Fig. 16. 3D point clouds of Configuration *A* during the tests.

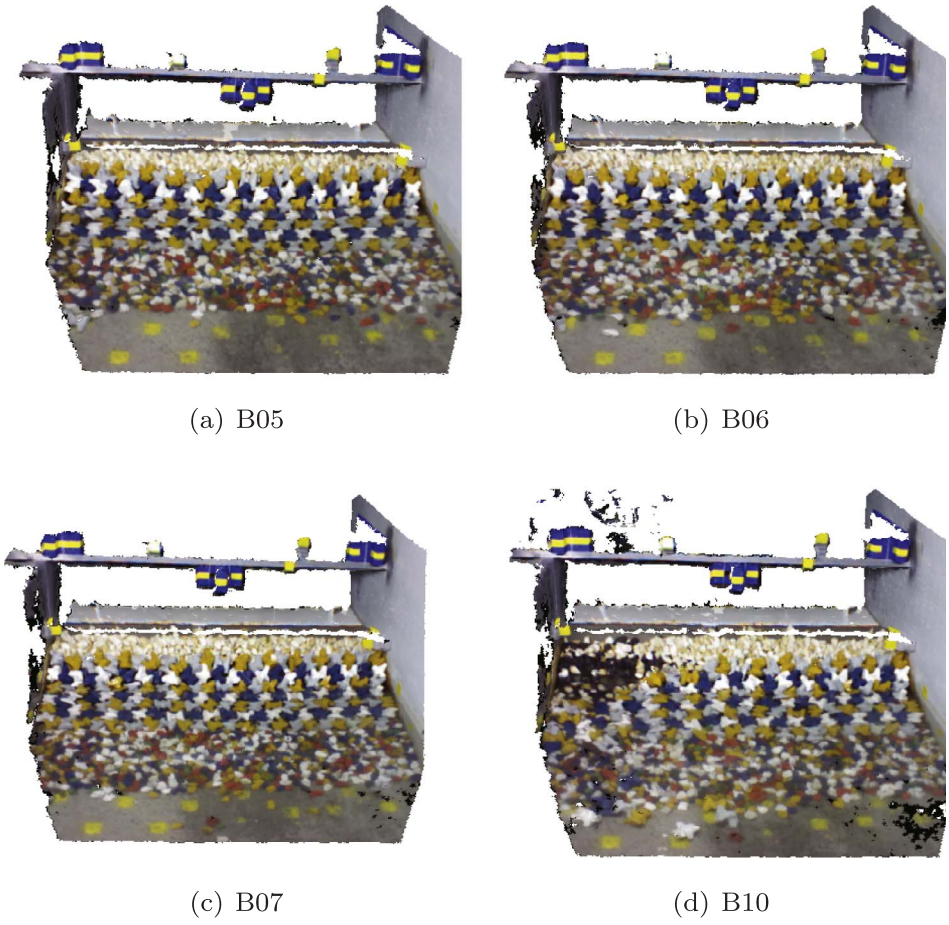

(a) B05 (b) B06

(c) B07 (d) B10

Fig. 17. 3D point clouds of Configuration *B* during the tests.

not possible to measure its dimensions. The relative error reaches its minimum (2%) with VVPM and VMIW set to 512 and 1000 respectively.

4. Experimental breakwater damage assessment

The aim of the experimental campaign was to demonstrate the advantages and the limits of the proposed methodology when applied to measure the damage of the armour layer of a breakwater at lab scale. To this aim, the stability of a traditional breakwater protected by an Accropode armour layer was investigated. The experiments were carried out at the Hydraulic Laboratory of the University of Catania. The wave tank is 18 m long, 3.60 m wide and 1.20 m deep. The flap-type wavemaker, located at one end of the flume, is electronically controlled and it is able to generate random waves with a given Jonswap spectrum. Fig. 14 shows a three-dimensional model of the wave tank. In the present experiments, in order to obtain a 2D behaviour of the structure, the full width of the tank was partitioned to obtain a wave flume 1 m wide where the physical model of the structure was located.

The Accropode elements are 4.64 cm high. They are made up of a mixture of synthetic resin, basaltic dust and iron sawdust. This mixture has both good moulding and drying characteristics, which facilitates the production of the elements. The density of the mixture is $\rho_r = 2303\ \mathrm{kg/m^3}$. In order to reduce scale effects induced by the roughness of the elements themselves, the Accropodes have been painted in different colours. The above technique is also traditionally used in laboratories to visually estimate the damage percentage N_d by counting the number of displaced elements. Fig. 15 shows the two configurations of the cross-section of the investigated breakwater. In both sections, the slope of the armour layer is 4:3, the core is made up of granulated marble stones, whose size is in the range $D = 9.0$–20.0 mm, and the filter layer is made up of basaltic quarry stone, with diameters in the range $D = 12.7$–15.0 mm. The toe of the two structures is different. Indeed, Configuration *A* has both the armour layer and the toe of the structure made up of Accropode elements, while the armour layer of Configuration *B* is protected by a berm made up of basaltic quarry stones, whose dimensions are in the range $D = 15.0$–20.0 mm. In this case, the offshore slope of toe berm is 3:2. Finally, in both cases, between the concrete seawall and the Accropode armour layer, an armouring of marble stones ($D = 30$ mm) is used. The breakwater was constructed by carefully following the building instructions for Accropode structures, in order to guarantee the maximum interlocking level [23]. This is essential in order to avoid any opening which could significantly influence the subsequent answer of the structure to the wave attack.

The characteristics of the incident and reflected wave motion were measured by means of a couple of resistive wave gauges, located 1.5 m off-shore of the toe of the structure. The well known two-gauge method was used to this aim [38]. The distance between the two wave gauges is about 0.17 m. The damage to the structure was monitored by means of both the RGB-D Kinect sensor and traditional optical systems. The latter was composed by a stabilised HDR-PJ10E Sony video camera (full HD recording mode), along with a Canon EOS 1000-D reflex camera. Both cameras were located on a steel frame perpendicularly to the breakwater model at a distance of about 1.2 m far from the toe of the structure, which is sufficient to obtain a good resolution and scan range [20].

Table 1 reports the tested wave conditions, in terms of the incident and reflected significant wave heights, H_{si} and H_{sr}, of the mean wave period, T_m, and of the reflection coefficient, K_r. The water depth at the wavemaker was equal to 0.30 m, while the water depth at the toe of the structure was equal to 0.17 m. Each test lasted about 1500 waves. For

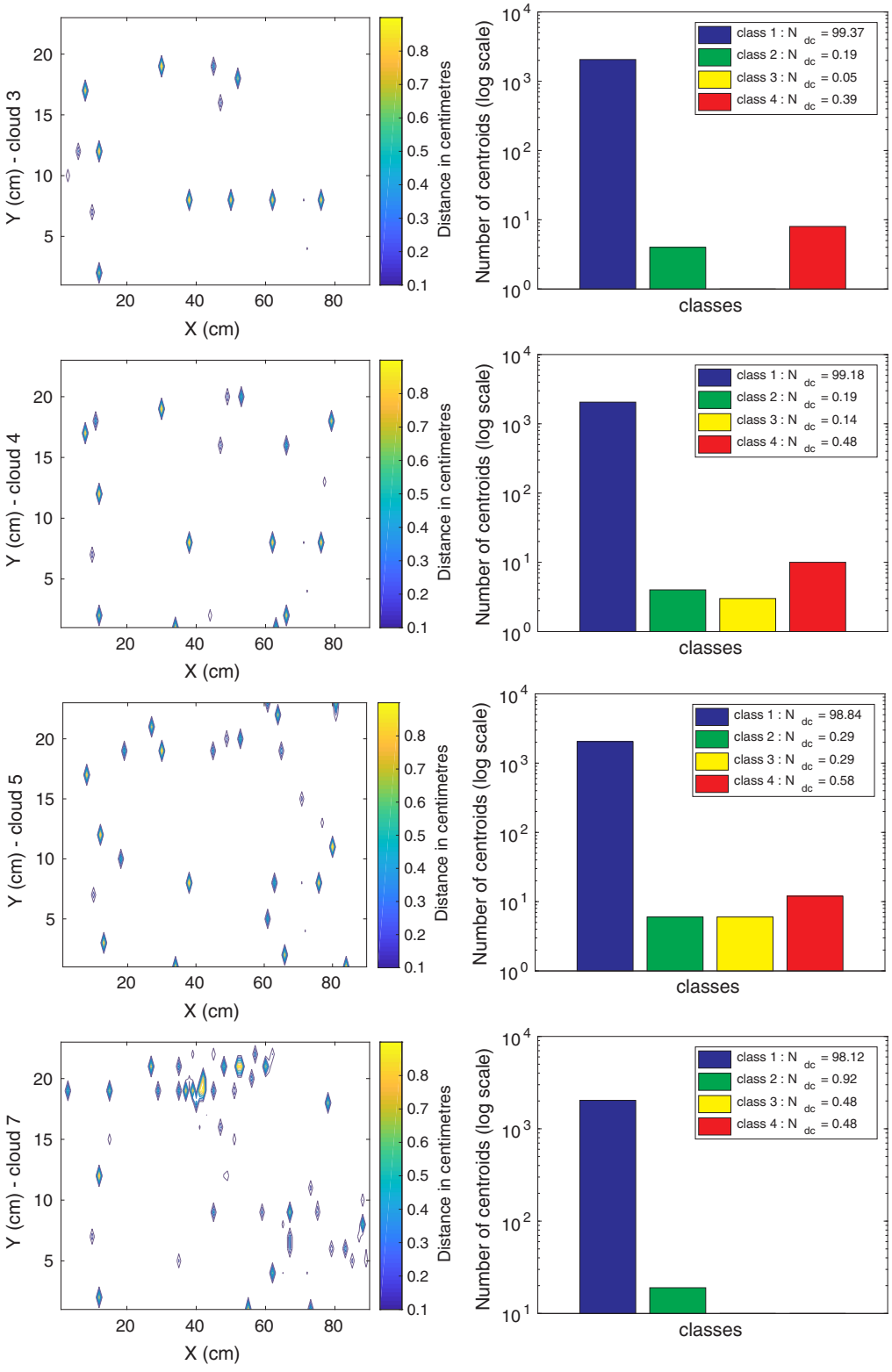

Fig. 18. Distance contour plots on X-Y plane from test sequence A (first column) along with N_{dc} bar plots (second column). Each row represents the following test clouds, in order from top to bottom: A03, A04, A05, A07.

both configurations *A* and *B*, shown in Fig. 15, a shake-down test was carried out in order to allow an adjustment of the structure similar to the one which occurs in the field due to small storms during construction [39]. The hydrodynamic conditions reported in Table 1 indicate that in both cases, the reflection coefficients are about 0.4, as expected for this type of structures [24]. It should be noted that the sequence of the waves of Configuration B was longer, since the structure resisted to more energetic waves.

5. Results of the 3D monitoring technique

A set of 3D point clouds of the breakwater gathered during the experiments are reported in Figs. 16 and 17, for Configurations *A* and *B*, respectively. Figs. 18 and 20 show the damage endured by the structure, visualised in terms of the Euclidean distance between the sampled control centroids (i. e. the control points obtained before the experiment started) and the centroids sampled at different instants during the

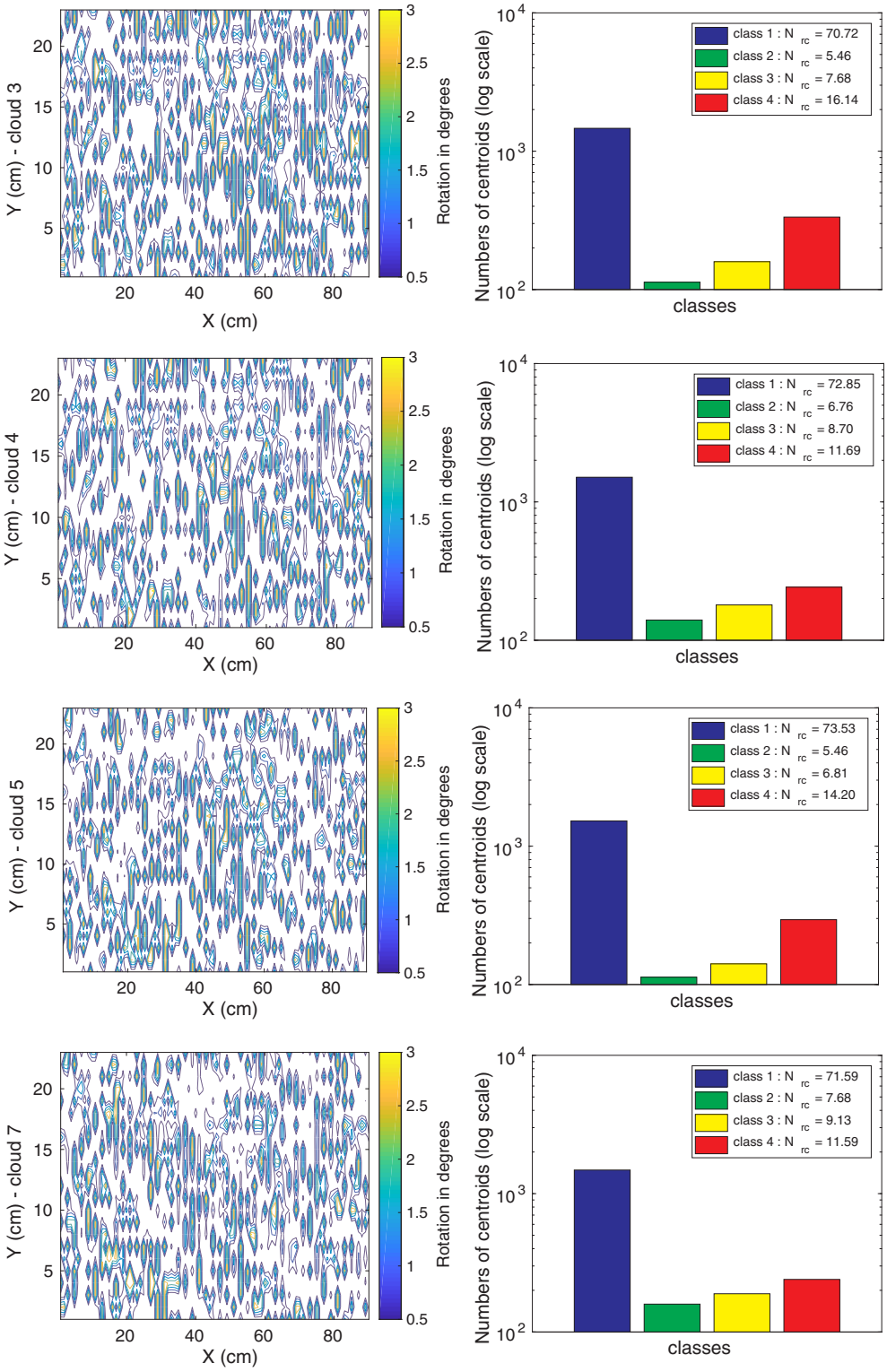

Fig. 19. Rotation contour plots on X-Y plane from test sequence A (first column) along with N_{rc} bar plots (second column). Each row represents the following test clouds, in order from top to bottom: A03, A04, A05, A07.

test. The first column of the Figures contains contour plots for the distances, projected on the X-Y plane, parallel to the plane of the armour layer. The second column reports bar plots for the damage parameter N_{dc}. Each row represents a cloud, that is a 3D model of the breakwater at different instants during the experiment.

The N_{dc} value is a measure of the overall damage of the breakwater based on the centroids distance. More precisely, it indicates the percentage of centroids, for a given cloud, whose shift lies in one of the selected distance classes. Every class represents a distance interval. The intervals are obtained by equally dividing the maximum registered distance by the number n of classes. Specifically:

$$class_d(i) = d:\ d \in \left[\frac{maxDistance}{n} \times (i-1), \frac{maxDistance}{n} \times i\right) \tag{5}$$

with $i \in \{1,2,\ldots,n\}$. When $i = n$, the $class_d$ set is fully closed, including therefore also the maximum distance. Finally, given a class i, we express N_{dc} with the following equation

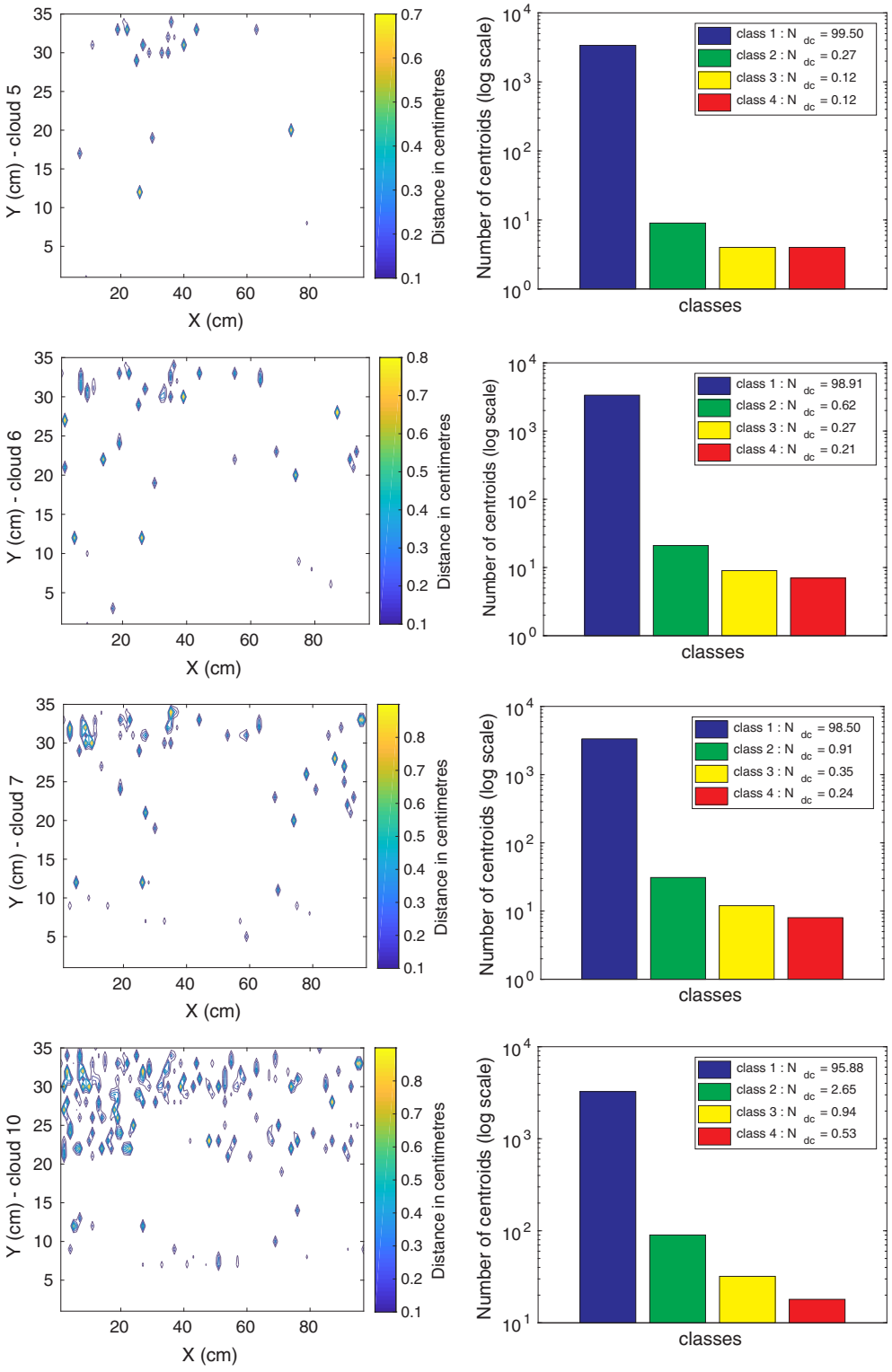

Fig. 20. Distance contour plots on X-Y plane from test sequence B (first column) along with N_{dc} bar plots (second column). Each row represents the following test clouds, in order from top to bottom: B05, B06, B07, B10.

$$N_{dc}^{i} = \frac{|\{c_t: d(c_t,c_c) \in class_d(i), c_t \in C_T\}|}{|C_T|} \tag{6}$$

where $d(c_t,c_c)$ is the distance between a test centroid c_t and its correspondent control centroid c_c, and C_T is the set containing all the test centroids. The control centroids do not belong to this set, as they are relative to the cloud acquired before the beginning of test. In the present analysis, the number of classes is $n = 4$. The definition of N_{dc} is very close to that of the damage percentage N_d. The main difference here is that while N_d refers to the individual block positions, which is somehow ambiguous to be determined, the parameter N_{dc} considers the positions of the centroids of the armour layer, which are automatically and unequivocally detected. Fig. 20 is a clear example of how the proposed methodology allows to easily track the status of the breakwater at a glance. As long as waves hit the barrier, Accropodes moved increasingly: at the beginning of the test (first three plots of the first row) only few Accropodes moved, while at the central and ending phase of the experiment many Accropodes were displaced (last row plots). We can observe that the upper region of the breakwater is the most

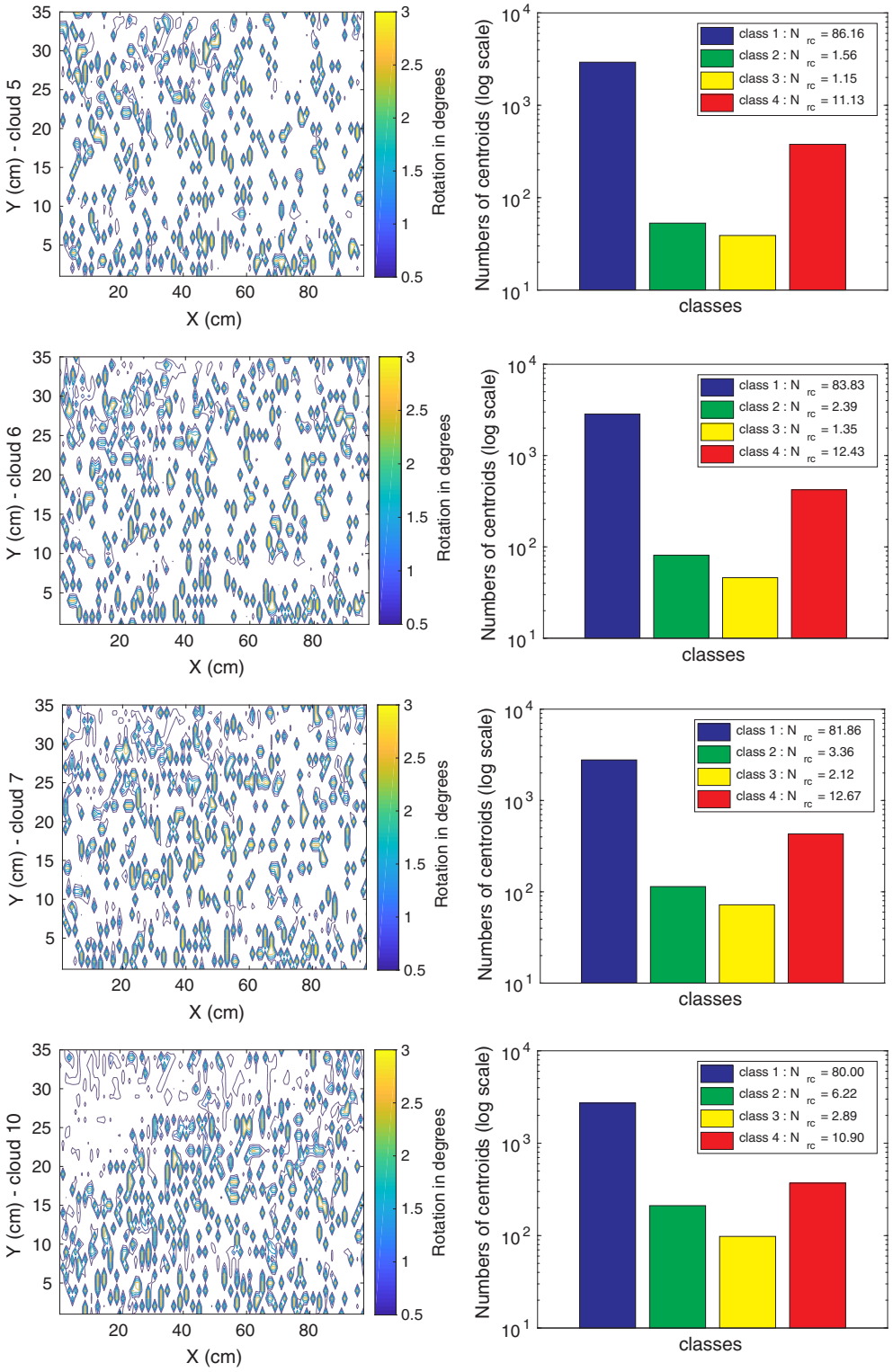

Fig. 21. Rotation contour plots on X-Y plane from test sequence B (first column) along with N_{rc} bar plots (second column). Each row represents the following test clouds, in order from top to bottom: B05, B06, B07, B10.

damaged part.

Figs. 19 and 21 show the damage of the same sequences expressed in terms of the rotation between the normal vectors of the control and test centroids. Both contour and bar plots are calculated as explained above. The only difference is that here the intervals between the different classes refer to the rotation angle between the centroids normals:

$$class_r(i) = r:\ r \in \left[\frac{maxRotation}{n} \times (i-1), \frac{maxRotation}{n} \times i\right) \tag{7}$$

$$N_{rc}^{i} = \frac{|\{c_t:\ r(c_t,c_c) \in class_r(i), c_t \in C_T\}|}{|C|} \tag{8}$$

where $r(c_t,c_c)$ is the rotation angle between the normal vector of a test centroid c_t and the normal vector of its correspondent control centroid c_c. In this case, $n = 4$ as well. The results on the rotational movements of the armour layer elements, albeit more noisy than the translation shifts plots, contribute to prove an incremental damage of the breakwater. The noise of rotational movements is mainly due to the fact we are estimating normals on very small region of the clouds (a sphere with

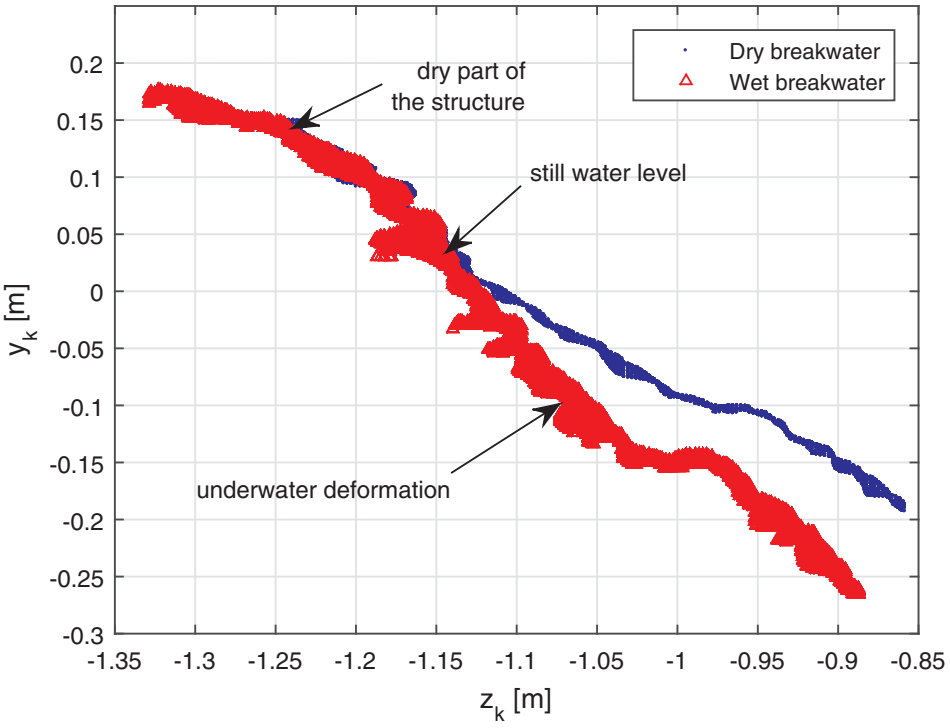

Fig. 22. Example of the cross-sections of the breakwater derived from the 3D point cloud in the absence of water (Dry breakwater) and in the presence of water. The transect is obtained at the centre of flume by considering a width of 2.86 cm.

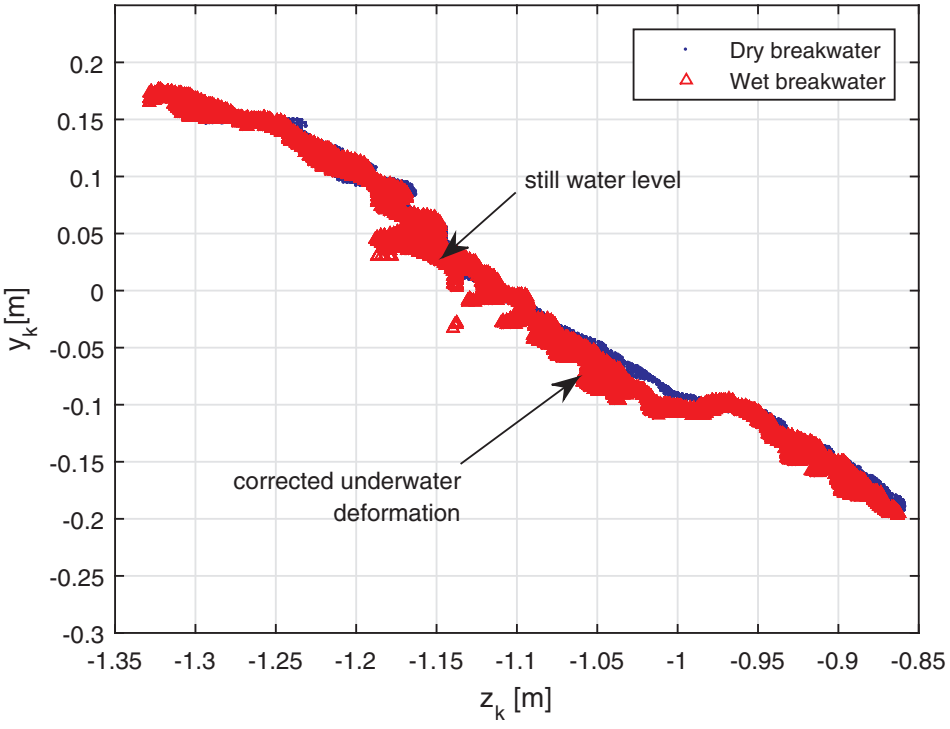

Fig. 23. Example of the same cross-sections of the breakwater shown in Fig. 22 obtained after applying a correction procedure to eliminate the deformation of the underwater part of the structure.

radius of 1 cm). Notice that the proposed monitoring technique allows an immediate and eventually even continuous monitoring of the evolution of the breakwater conditions.

6. Results derived from the 3D technique using traditional methods

Traditionally, the damage assessment of rubble mound breakwaters is performed by considering the damage level $S = A_e/D_n^2$, with A_e being the eroded area of a reference cross-section of the structure and D_n being the nominal diameter of the blocks. The easiest way to measure the 2D cross-section of the structure and its deformation is to monitor it through the glass wall of the flume, i.e. just considering the lateral part of the breakwater.

The 3D point clouds obtained by the Kinect camera can be used to determine the 2D cross-section of the armour layer and, in turn, to derive the damage level S at any section in the transversal direction of the flume. In particular, since the cloud points are randomly distributed, the shape of a generic section is obtained by considering a transect of the clouds, with a fixed width. Fig. 22 shows an example of

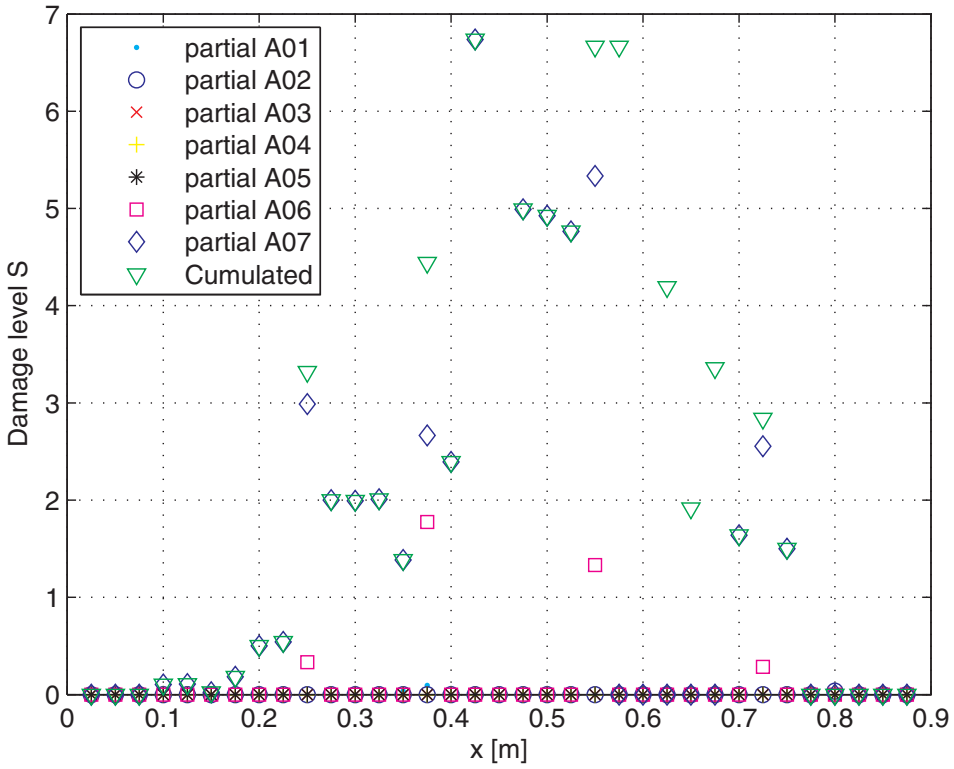

Fig. 24. Partial and cumulated damage level calculated considering 35 cross-sections of the Configuration *A* of the breakwater.

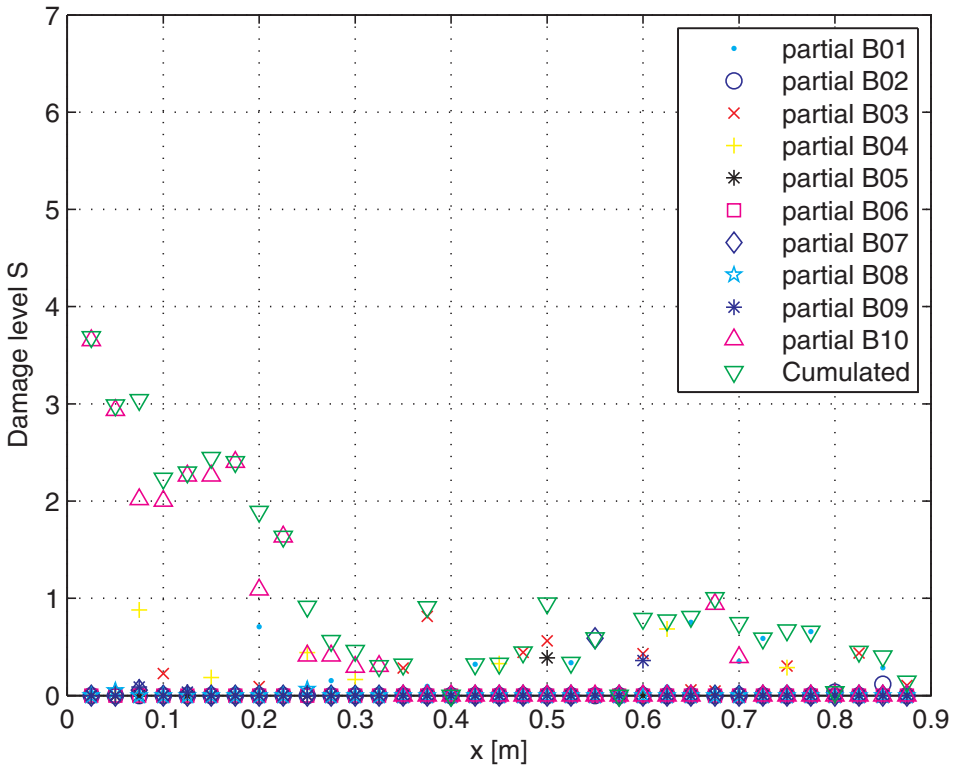

Fig. 25. Partial and cumulated damage level calculated considering 35 cross-sections of the Configuration *B* of the breakwater.

the cross section of the Configuration *B* of the breakwater derived from the Kinect measurements both in the absence and in the presence of water at the centre of the flume. Clearly, the emerged part of the two measured sections overlaps, whereas optical refraction causes a deformation below water level. A correction of such a deformation is carried out by considering a rotation angle α and a scaling factor f of the submerged part of the section. In order to minimise the errors, the optimal values of such parameters turned out to be $\alpha = 0.16$ rad and $f = 0.93$. An example of the result of the above transformation is reported in Fig. 23. Figs. 24 and 25 show the damage levels calculated considering 35 cross-sections, obtained along the entire width of Configuration *A* and Configuration *B* of the breakwater respectively. In particular, both the partial damage parameter calculated at the end of each tested sea-state and the cumulated damage levels are shown in the

Figures. Table 1 reports the values of the stability number N_s of the performed experiments, calculated by assuming that the nominal diameter D_n is equal to 0.7 of the height of the Accropode blocks. It can be observed that in both cases the structure shows a strong three-dimensional behaviour. For example, Configuration *A* appears to be stable up to wave condition A05 ($N_s = 3.92$), while the damage starts in the central part of the structure for $N_s = 3.96$ (test A06), by attaining damage levels close to $S = 2$. Once started, the damage cannot be arrested, even though the waves are slightly less energetic ($N_s = 3.81$ in test A07), and it extends to the other parts of the armour layer. The above results agree with the criteria suggested by van der Meer [4], who for Accropode structures predicted start of damage for $N_s > 3.7 \pm 0.2$ and failure for $N_s > 4.1 \pm 0.2$.

The beneficial effects of the presence of the berm at the toe is confirmed by the results shown in Fig. 25. In fact, compared to Configuration *A*, Configuration *B* seems to be much more resilient to wave attack, since the damage level remains quite small up to $N_s = 6.10$ (test B10). In particular, it may be noticed that small movements of the blocks are present over the entire length of the structure during tests B01-B04 (i.e. up to $N_s = 5.14$), with damage levels smaller than 1. Probably such movements allowed the Accropode armour layer, which is supported by the irregular quarry-stone berm, to adjust itself and to reach a more stable configuration. Indeed, almost everywhere the damage levels drop to zero during tests B05-B09, proving the fact that no deformations of the structure are observed. Finally, during test B10, the structure fails at the lateral left side. Contrary to what happened for the Configuration *A*, where the failure was progressive, in this case the failure was much quicker, with exposure of the filter layer.

7. Conclusions

A novel approach to measure the damage to rubble mound breakwaters simultaneously above and below the sea water level is proposed. The developed methodology is based on the fully automatic analysis of 3D point clouds of the armour layers subject to sequences of wave attack.

Considering a sub-cloud sampling of the static part of the scene, the proposed algorithm automatically aligns all the point clouds by using the Iterative Closest Point algorithm. Then, the deformation of the armour layer is evaluated in terms of translations and rotations of its surface. The initial position of the structure is used as a reference, while the armour layer is subsampled considering the centroids of the cloud point contained in cubes of size 2 cm.

The above methodology is applied to 3D depth maps of two configurations of an Accropode breakwater recorded by a budget RGB-D camera which uses IR structured light, namely the well known Microsoft Kinect camera. The system does not need a preliminary calibration. Accropode structures represent an ideal case for testing the capabilities of the system, since their stability can be compromised by very small movements of the armour layer elements, which thus need to be accurately measured. A preliminary analysis is performed in order to optimise the setting parameters of the Kinect sensor (VVR, VVPM, VMIW, etc.), the positioning of the camera with respect to the structure, and the measurement errors of the system. The analysis reveals that at a distance from the breakwater of about 1 m it is possible to reach measurement errors smaller than 0.003 m.

In order to investigate the advantages and disadvantages of the proposed methodology, we carried out tests at a lab scale on two configurations of an Accropode breakwater, with different design of the toe of the structure, and in turn different stability properties of the armour layer. Both structures are attacked by series of sea states, made up by about 1500 irregular waves, having increasing and then decreasing wave energy. Such forcing mimics the conditions during typical storms.

Two parameters, N_{dc}^i and N_{rc}^i, are introduced and used to quantify and cluster the damage of different parts of the structure. The first one, which measures the damage to the structure in terms of translational displacements, is very similar to the classical damage percentage N_d. However, while the latter provides an integral measure of the damage and its calculation may be computationally expensive, N_{dc}^i is univocally defined and automatically calculated. In the present application, a clear three-dimensional behaviour of the structure is observed. The use of N_{dc}^i provides a clear representation of the spatial and temporal evolution of the breakwater damage, by allowing one to point out the area where the structure damage is initiated and in turn to locate the weakest region of the armour layer. The results obtained by using N_{dc}^i agree quite well with the damage estimate of the widely-used damage parameter *S*, which can be determined using the same point cloud results. The parameter N_{rc}^i, which provides a measure of the rotational movements of the elements of the armour layer, has never been considered before and it is an useful parameter to assess not only structural damage but also the degrees of freedom of the blocks and their attitude to become unstable, which could eventually leads to failure.

From the above results, it appears that the proposed methodology permits an immediate and eventually even continuous detailed monitoring of the breakwater status, simultaneously above and below the sea water level, using low-cost RGB-D technologies. It follows that the advantages for laboratory investigation of the stability of rubble mound breakwaters are clearly significant, in terms of operational time, economical costs, and of possibilities of testing alternative configurations.

Future developments of the technique will include testing in dynamic conditions, i.e. in the presence of the moving water surface also in order to relate camera parameters to the initiation of motion of the elements of the armour layer and to its local actuators. Additionally, it should be mentioned that RGB-D technologies have potential to be applied to field conditions. Indeed, the survey of the actual status of a breakwater is a complex task with an high safety risk associated to it at present, mainly because of the visual inspection of submerged part of the structure usually carried out by professional scuba divers. The use of remote local sensing techniques, such as RGB-D camera able to recover at the same time the sub-aerial and submerged parts of the structure and which could be located on boats without worries about the movement of the sensor, could be thus highly beneficial.

Acknowledgements

This work has been partly funded by the European Commission, project HYDRALAB PLUS (contract No. 654110).

References

[1] F. Dentale, G. Donnarumma, E. Pugliese Carratelli, Simulation of flow within armour blocks in a breakwater, J. Coast. Res. 30 (3) (2014) 528–536.
[2] R. Hudson, Laboratory investigation of rubble mound breakwaters, J. Waterways Harbors Div. 85 (1959) 93–122.
[3] J. van der Meer, Stability of breakwater armour layers - Design formulae, Coast. Eng. 11 (1987) 219–239.
[4] J. van der Meer, Stability of cubes, tetrapods and accropode, in: Breakwater '88, 1988.
[5] J. van der Meer, Design of concrete armour layers, Proc. Coastal Structures '99, Balkema Rotterdam, 1999, pp. 213–221.
[6] M. Kramer, B. Zanuttigh, J.V. der Meer, C. Vidal, F. Gironella, Laboratory experiments on low-crested breakwaters, Coast. Eng. 52 (2005) 867–885.
[7] H. Burcharth, M. Kramer, A. Lamberti, B. Zanuttigh, Structural stability of detached low crested breakwaters, Coast. Eng. 53 (2006) 381–394.
[8] C. Vidal, R. Medina, P. Lomonaco, Wave height parameter for damage description of rubble-mound brekwaters, Coast. Eng. 53 (2006) 711–722.
[9] M. van Gent, Oblique wave attack on rubble mound breakwaters, Coast. Eng. 88 (2014) 43–54.
[10] C. Vidal, F. Martin, V. Negro, X. Gironella, B. Madrigal, J. Garcia-Palacios, Measurement of armor damage on rubble mound structures: comparison between different methodologies, in: Coastal Structure, 2003.
[11] K. Cihan, Y. Yuksel, Deformation of breakwater armoured artificial units under cyclic loading, Appl. Ocean Res. 42 (2013) 79–86.
[12] M. van Gent, Rock stability of rubble mound breakwaters with a berm, Coast. Eng. 78 (2013) 35–45.
[13] H. Guler, T. Arikawa, T. Oei, A. Yalciner, Performance of rubble mound breakwaters under tsunami attack, a case study: Haydarpasa port, Istanbul, Turkey, Coast. Eng. 104 (2015) 43–53.

[14] S. Eslami, M. van Gent, Wave overtopping and rubble mound stability under combined loading of waves and current, in: ICCE 2010, 2010.
[15] K. Cihan, Y. Yuksel, Deformation of rubble-mound breakwaters under cyclic loads, Coast. Eng. 58 (2011) 528–539.
[16] F. Comola, T.L. Andersen, L. Martinelli, H. Burcharth, P. Ruol, Damage pattern and damage progression on breakwater roundheads under multdirectional waves, Coast. Eng. 83 (2014) 24–35.
[17] M. Martin-Hidalgo, M.J. Martin-Soldevilla, V. Negro, P. Aberturas, J. Lopez-Gutierrez, Storm evolution characterization for analysing stone armour damage progression, Coast. Eng. 85 (2014) 1–11.
[18] B. Chilo, F. Guiducci, Computerised methodology to measure rubble mound brekwater damage, in: Proccedings of the 24th Conference on Coastal Engineering, Kobe, Japan, 1994.
[19] M. van Gent, I. van der Werf, Rock toe stability of rubble mound breakwaters, Coast. Eng. 83 (2014) 166–176.
[20] F. Marinello, A. Pezzuolo, F. Gasparini, J. Arvidsson, L. Sartori, Application of the kinect sensor for dynamic soil surface characterization, Precis. Agric. 16 (6) (2015) 601–612.
[21] H. Shen, B. He, J. Zhang, S. Chen, Obtaining four-dimensional vibration information for vibrating surfaces with a kinect sensor, Measurement 65 (2015) 149–165.
[22] M. Bueno, L. Díaz-Vilariño, J. Martínez-Sánchez, H. González-Jorge, H. Lorenzo, P. Arias, Metrological evaluation of kinectfusion and its comparison with microsoft kinect sensor, Measurement 73 (2015) 137–145.
[23] V. Verma, K. Varghese, A. Sekar, Evaldamage of physical modeling and 3-d simulation of planning Accropode placements, in: ISARC 2004 21st International Symposium on Automation and Robotics in Construction, 2004.
[24] M. Kobayashi, S. Kaihatsu, Hydraulic characteristics and field experience of new wave dissipating concrete blocks (ACCROPODE), in: Proceedings of 19th Conference on Coastal Engineering, 1984.
[25] J. van der Meer, Conceptual design of rubble mound breakwaters, in: A.N. York (Ed.), Proceedings of a Short Course on the Design and Reliability of Coastal Structures, 23rd Conf. Coastal Eng., Venice, 1992, pp. 447–510.
[26] B. Tippetts, D.J. Lee, K. Lillywhite, J. Archibald, Review of stereo vision algorithms and their suitability for resource-limited systems, J. Real-Time Image Process. (2013) 1–21.
[27] D. Fofi, T. Sliwa, Y. Voisin, A comparative survey on invisible structured light, in: Electronic Imaging 2004, International Society for Optics and Photonics, 2004, pp. 90–98.
[28] S. Baglio, E. Foti, R. Musumeci, Measuring the effects of wave action around piers, IEEE Instrum. Meas. Mag. 8 (5) (2005) 28–33.
[29] E. Foti, I. Caceres-Rabionet, A. Marini, R. Musumeci, A. Sanchez-Arcilla, Experimental investigation of the bed evolution in wave flumes: performance of 2D and 3D optical systems, Coast. Eng. 58 (7) (2011) 606–622.
[30] W. Jang, C. Je, Y. Seo, S.W. Lee, Structured-light stereo: comparative analysis and integration of structured-light and active stereo for measuring dynamic shape, Opt. Lasers Eng. 51 (11) (2013) 1255–1264.
[31] S.B. Gokturk, H. Yalcin, C. Bamji, A time-of-flight depth sensor-system description, issues and solutions, Conference on Computer Vision and Pattern Recognition Workshop, 2004, CVPRW'04, IEEE, 2004, p. 35.
[32] J. Zhu, L. Wang, R. Yang, J. Davis, Fusion of time-of-flight depth and stereo for high accuracy depth maps, IEEE Conference on Computer Vision and Pattern Recognition, 2008, CVPR 2008, IEEE, 2008, pp. 1–8.
[33] Y. Chen, G. Medioni, Object modelling by registration of multiple range images, Image Vis. Comput. 10 (3) (1992) 145–155.
[34] J.L. Bentley, Multidimensional binary search trees used for associative searching, Commun. ACM 18 (9) (1975) 509–517.
[35] J. Berkmann, T. Caelli, Computation of surface geometry and segmentation using covariance techniques, IEEE Trans. Pattern Anal. Mach. Intell. 16 (11) (1994) 1114–1116.
[36] Z. Zhang, Microsoft kinect sensor and its effect, IEEE MultiMedia 19 (2) (2012) 4–10.
[37] S. Izadi, D. Kim, O. Hilliges, D. Molyneaux, R. Newcombe, P. Kohli, J. Shotton, S. Hodges, D. Freeman, A. Davison, et al., Kinectfusion: real-time 3d reconstruction and interaction using a moving depth camera, Proceedings of the 24th Annual ACM Symposium on User Interface Software and Technology, ACM, 2011, pp. 559–568.
[38] Y. Goda, Y. Suzuki, Estimation of incident and reflected waves in random wave experiments, in: Proceedings of 15th International Conference on Coastal Engineering, 1976, pp. 828–845.
[39] G. Wolters, W. Allsop, L. Hamm, D. Mühlestein, M. van Gent, L. Bonthoux, J. Kirkegaard, R.C. Ao, J. Fortes, X. Gironella, L. Pinheiro, J. Ao Santos, I. Sousa, Users Guide to Physical Modelling and Experimentation, Experience of the HYDRALAB Network, CRC Press, Taylor and Francis Group, Ch. Breakwaters, 2011, pp. 39–66.